

Superscaling in the resonance region for neutrino-nucleus scattering: The SuSAv2 dynamical coupled-channels model

J. Gonzalez-Rosa¹, G. D. Megias¹, J. A. Caballero^{1,2}, M. B. Barbaro^{3,4} and J. M. Franco-Patino^{1,3,4}

¹*Departamento de Física Atómica, Molecular y Nuclear, Universidad de Sevilla, 41080 Sevilla, Spain*

²*Instituto de Física Teórica y Computacional Carlos I, Granada 18071, Spain*

³*Dipartimento di Fisica, Università di Torino, Via P. Giuria 1, 10125 Torino, Italy*

⁴*INFN, Sezione di Torino, Via P. Giuria 1, 10125 Torino, Italy*



(Received 20 June 2023; accepted 20 November 2023; published 20 December 2023)

In this work, the SuSAv2 and dynamical coupled-channels (DCC) models have been combined and tested in the inelastic regime for electron and neutrino reactions on nuclei. The DCC model, an approach to study baryon resonances through electron and neutrino induced meson production reactions, has been implemented for the first time in the SuSAv2-inelastic model to analyze the resonance region. Within this framework, we also present a novel description about other inelasticities in the resonance region (SoftDIS). The outcomes of these approaches are firstly benchmarked against (e, e') data on ^{12}C . The description is thus extended to the study of neutrino-nucleus inclusive cross sections on ^{12}C and ^{40}Ar and compared with data from the T2K, MicroBooNE, ArgoNEUT, and MINERvA experiments, thus covering a wide kinematical range.

DOI: [10.1103/PhysRevD.108.113008](https://doi.org/10.1103/PhysRevD.108.113008)

I. INTRODUCTION

The description of neutrino-nucleus reactions is essential for the analysis of neutrino oscillation experiments and the determination of relevant properties, such as the violation of the charge-parity symmetry in the neutrino sector and the mass hierarchy [1]. These studies are of paramount relevance to reduce one of the leading experimental systematics, the cross section and neutrino flux determination, which is strongly related to nuclear-medium uncertainties. Most of past, current, and future experiments—MiniBooNE, MicroBooNE, T2K, NOvA, MINERvA, ArgoNEUT, DUNE, and HyperK—[2–12] operate in the 0.5–10 GeV region, where different channels play a relevant role in the nuclear response. The quasielastic (QE) regime, associated to one-nucleon knockout, is a very prominent contribution in the range from hundreds of MeV to a few GeV of initial neutrino energy. In this region, it is also necessary to consider the emission of two nucleons, denoted as 2p2h (two-particle-two-hole) channel, and the resonance (RES) regime, corresponding to the excitation of nucleonic resonances followed by their decay and the subsequent emission of pions and other mesons. As the neutrino energies increase up to several GeV, not only the resonance regime but also

other inelasticities, corresponding to nonresonant meson production and deep-inelastic scattering (DIS) processes, become more relevant. This energy domain is of interest for some of the above-mentioned experiments, such as MINERvA or ArgoNEUT, and will be essential for the next-generation DUNE experiment. Although most of current measurements are focused on the $\text{CC}0\pi$ (or “quasielasticlike”) channel, which is defined as charged-current (CC) reactions with no pions (0π) detected in the final state and, thus, dominated by QE and 2p2h contributions, the inelastic region is also accessed in some of these experiments via CC-inclusive measurements, where no specific hadronic final state is selected, and hence, all reaction mechanisms have to be considered. The inelastic regime, which includes resonant and nonresonant meson production and deep-inelastic scattering, can also represent an important background in $\text{CC}0\pi$ data.

The resonance regime has been extensively studied in previous works by different groups [9,13–20]. Emphasis has been placed not only on the description of the nucleonic resonances but also on the treatment of the nuclear effects introduced in the analysis of lepton-nucleus reactions. Moreover, there is a lack of accurate models and specific measurements in the so-called shallow inelastic scattering (SIS) region, that is, the transition region between the resonant and DIS regimes [1,21,22]. Information about the resonant nucleon form factors and the inelastic structure functions is mainly extracted from electron scattering data, which implies some restrictions when extended to the neutrino case, as the axial channel is missing in electron

Published by the American Physical Society under the terms of the Creative Commons Attribution 4.0 International license. Further distribution of this work must maintain attribution to the author(s) and the published article's title, journal citation, and DOI. Funded by SCOAP³.

reactions. This extension thus requires relying on different approximations based on QCD calculations, quark models, and parton distribution functions (PDFs) or semiphenomenological models. Nonetheless, most of these approaches are affected by kinematical restrictions and large uncertainties, which makes it difficult to get a consistent and accurate description of the full inelastic regime. The SIS and DIS channels have been investigated in several recent studies [13,14,19,20,23–29] but, up to present, no satisfactory models have been fully developed in the kinematics of interest for oscillation experiments.

More specifically, several groups [18,30–35] have studied pion production in nuclei, providing different descriptions of the initial nuclear state, pion production in a bound nucleon, and the possible subsequent pion-nucleon interaction within the residual nucleus. Most of the initial studies were based on the simple Fermi gas approach of noninteracting nucleons, but recently more sophisticated descriptions have been developed, incorporating relativistic mean field nuclear potentials, Random phase approximation calculations or spectral functions. Regarding resonant production in the nucleon, several groups have also developed sophisticated approaches to analyze the nucleon structure in this regime, such as the M. Kabirmezhad single-pion production model [36,37] or the dynamical coupled-channels (DCC) model [38–40], which have been tested against electron and neutrino scattering data, being also recently implemented in the extended factorization scheme [41].

In a recent work [42], the superscaling model SuSAv2, initially developed for CCQE neutrino-nucleus cross sections, was extended to the full inelastic regime (SuSAv2-inelastic), where the resonance production and deep inelastic contributions were described via the extension to the neutrino sector of the SuSAv2 inelastic model developed for (e, e') reactions [43]. The model merges inelastic structure functions [44–52], coming from QCD analyses, parton distribution functions (PDFs) or phenomenological approaches, with a mean-field nuclear scaling function to describe the nuclear dynamics. This approach also allows one to discriminate between different inelastic regions by introducing some restrictions in the allowed final-state invariant mass. For example, a semiphenomenological Δ resonance model based on the scaling function extracted from (e, e') data was also developed and combined with the SuSAv2-inelastic model after removing this resonant contribution from the latter. The comparison with both electron and neutrino data was rather satisfactory.

With the aim of studying the sensitivity of these results to different inputs for the elementary lepton-nucleon inelastic structure functions, in this work, we implement the DCC model to describe the resonant and nonresonant channels in lepton-nucleon interactions within the SuSAv2-inelastic nuclear framework described above. The DCC model has been widely tested for electron and neutrino scattering off a single nucleon and has the merit of considering a rather

complete description of the resonant and nonresonant regimes, also including the interaction between the different resonance channels (πN , $\pi\pi N$, ηN , $K\Lambda$, $K\Sigma$), the interference between resonant and nonresonant amplitudes and the neutrino induced two-pion production. Thus, in this work, the description of the structure functions related to the resonant and nonresonant regimes is provided by the DCC model, that can be obtained from [40], while using the inelastic structure functions employed in the former SuSAv2-inelastic model at higher kinematics (SIS and DIS) [42,43]. Note that the DCC model allows us either to consider only the contributions coming from pions (π -DCC) or the so-called inclusive contribution (inclusive-DCC) that includes a more complete description of the resonant and nonresonant regimes as defined above.

The DCC model implemented within the SuSAv2 framework is denoted as SuSAv2-DCC. In the case of the DCC model, we explore different prescriptions for the inelastic structure functions. This also allows us to quantify the contribution of the DIS/SIS channel to the resonant and nonresonant regimes by subtracting the SuSAv2-DCC contribution from the full inelastic prediction. This is denoted as “Soft-DIS” in this work and is connected with the SIS region.

All these approaches are described in Sec. II, where the theoretical formalism for the inelastic regime is also summarized and a comparison of the DCC parametrization and the different inelastic structure functions available in the SuSAv2-inelastic framework is presented. In Sec. III, we show the comparison of our predictions with data: in Sec. III A, the analysis of electron reactions on ^{12}C is shown as a first benchmark to test the validity of the approaches before applying them to the neutrino case; in Sec. III B, a comparison with CC-inclusive neutrino cross section measurements on ^{12}C and ^{40}Ar is presented at different kinematics and for several experiments. In Sec. IV, we draw our conclusions.

II. THEORETICAL BACKGROUND

The superscaling approach (SuSA) is based on the scaling properties exhibited by inclusive electron scattering where the QE scattering cross section can be written, under certain conditions, as a term containing the single-nucleon cross section times a scaling function (f) that embodies the nuclear dynamics. The analysis of inclusive electron scattering data [53] has shown that, for not too low transferred momentum (q larger than about 400 MeV/c), the scaling function does not depend on q (scaling of the first kind) nor on the nuclear species (scaling of the second kind) and can therefore be expressed in terms of a single variable ψ , the so-called scaling variable. A more detailed description of superscaling can be found in [43,53–59]. This approach has been also successfully applied to inclusive CCQE neutrino scattering and, most recently, to the full inelastic regime for both electron and neutrino

reactions. The description of the 2p2h channel has also been included in the model on the basis of the fully relativistic calculation of [60,61]. The corresponding model for the quasielastic region (SuSAv2-QE) is based on a set of QE scaling functions extracted from the relativistic mean field (RMF) model for the nucleus.

The SuSAv2-inelastic model is an extension of the SuSAv2-QE approach to the inelastic regime [42,62]. The double differential inclusive cross section for lepton-nucleus scattering with respect to transferred energy ω and the scattered lepton solid angle Ω can be written in the very general form [54],

$$\frac{d\sigma}{d\Omega d\omega} = \sigma_0 \sum_K v_K R_K, \quad (1)$$

where σ_0 is an elementary cross section (the Mott cross section in the case of electron scattering), v_K are kinematic Rosenbluth factors, and R^K are the nuclear response functions, containing all the nuclear dynamics. The summed index K is associated to different components of the nuclear tensor with respect to the direction of the transferred momentum \mathbf{q} . The nuclear responses depend on the transferred momentum and energy (q, ω) and on the invariant mass $W_X \equiv m_N \mu_X$ of the hadronic final states. In the SuSAv2-inelastic model, they are given by

$$R_K^{\text{inel}}(q, \omega, W_X) = N \frac{2T_F m_N^3}{k_F^3 q} \int_{\mu_X^{\text{min}}}^{\mu_X^{\text{max}}} d\mu_X \mu_X f^{\text{model}}(\psi_X) G_K^{\text{inel}}, \quad (2)$$

being N the number of nucleons participating to the reaction, k_F the Fermi momentum and $T_F \equiv \sqrt{m_N^2 + k_F^2} - m_N$ the Fermi kinetic energy. Thus, the inelastic nuclear responses are defined as the integral over all possible final hadronic states of the single-nucleon inelastic hadronic tensor G_K^{inel} times the inelastic scaling function f^{model} evaluated in a given nuclear model. The latter is written in terms of $\psi_X \equiv \psi_X(q, \omega, W_X)$, which is the extension of the QE scaling variable ψ to the inelastic regime and now depends on the final state invariant mass W_X . The limits of the integral ($\mu_X^{\text{min/max}}$) depend on the kinematics, on the specific inelastic channel (full inelastic, DIS, RES, etc.) and on the range of validity of the inelastic structure functions used to evaluate the single-nucleon tensor. These limits can also be altered to mix different models, avoiding double counting.

In previous works [42,43], we have employed either phenomenological inelastic structure functions [Bodek-Ritchie (BR), Bosted-Christy (BC)] or parton distribution functions (GRV98) [47,48,63–70] to analyze the full inelastic regime, and we have also addressed their extension to the neutrino sector. However, the ranges of validity of these approaches are quite different from each other and not all of them are accurate to describe the resonant and non-resonant

regimes. Specifically, BC works well for $Q^2 < 8 \text{ GeV}^2$ and $1.1 < W_X/\text{GeV} < 3.1$, PDF for high Q^2 ($0.8 < Q^2/\text{GeV}^2 < 10^6$) and $W \gtrsim 3 \text{ GeV}$, and BR covers a Q^2 range from 0.1 to 30 GeV^2 . The above-mentioned DCC model for pion production shows a range of validity within $W_X < 2.1 \text{ GeV}$ and $Q^2 < 3.0 \text{ GeV}^2$. In Fig. 1, where the inelastic neutrino-nucleon structure function F_1 is displayed versus the invariant mass, the differences between these approaches can be clearly noticed: BR and BC describe the resonant structures observed in the inelastic regime and moderate kinematics with a monotonic tail corresponding to DIS, while PDF only predicts an average of the resonance region [71]. On the contrary, the DCC model describes the resonant structures, but the results rapidly decrease after the resonance region as no deep-inelastic scattering contributions are considered, being thus consistently below the predictions of the other approaches. As we observe in Fig. 1, the π -DCC curve has less strength than the inclusive-DCC one that incorporates other contributions beyond the 1π emission. In what follows, when mentioning the DCC model, we refer only to the inclusive resonance structure functions given from [40].

Accordingly, in this work, we split the inelastic contributions in three parts. First, to address resonant and non-resonant pion production, we make use of the DCC model, setting the limits of the integral of Eq. (2) to $W_X^{\text{min}} = m_N + m_\pi$ and $W_X^{\text{max}} = 2.1 \text{ GeV}$, according to the validity range given by [38]. Above $W_X = 2.1 \text{ GeV}$, we make use of the inelastic structure functions mentioned in Sec. I to describe the DIS regime. Furthermore, Fig. 1 clearly shows that there are still inelastic processes not accounted for by the DCC approach below $W_X = 2.1 \text{ GeV}$. In this case, we consider DIS contributions both above the resonance region described by DCC (“TrueDIS”) and within this resonance region (“SoftDIS”). For TrueDIS, the limits are $W_X^{\text{min}} = 2.1 \text{ GeV}$ and $W_X^{\text{max}} = m_N + \omega - E_s$, being E_s the separation energy. The SoftDIS contribution shares the limits of the resonance region but, in order to avoid double counting, we subtract in the SuSAv2-inelastic approach the contribution from the SuSAv2-DCC model applied to the resonance regime (up to $W_X = 2.1 \text{ GeV}$). Thus, Soft-DIS contribution is defined as

$$\left(\frac{d^2\sigma}{d\Omega dk_l} \right)_{\text{SoftDIS}} = \left(\frac{d^2\sigma}{d\Omega dk_l} \right)_{\text{inelastic}}^{W_X^{\text{min}}=m_N+m_\pi; W_X^{\text{max}}=2.1 \text{ GeV}} - \left(\frac{d^2\sigma}{d\Omega dk_l} \right)_{\text{RES-DCC}}. \quad (3)$$

In order to define the nuclear responses within the DCC model, the functional form of the scaling function $f^{\text{model}} \equiv f^{\text{DCC}}$ and the inelastic scaling variable ψ_X shown in Eq. (2) are the same as used for the SuSAv2-inelastic model, and detailed in [42,43], being the only difference the kinematic region of applicability of the DCC model.

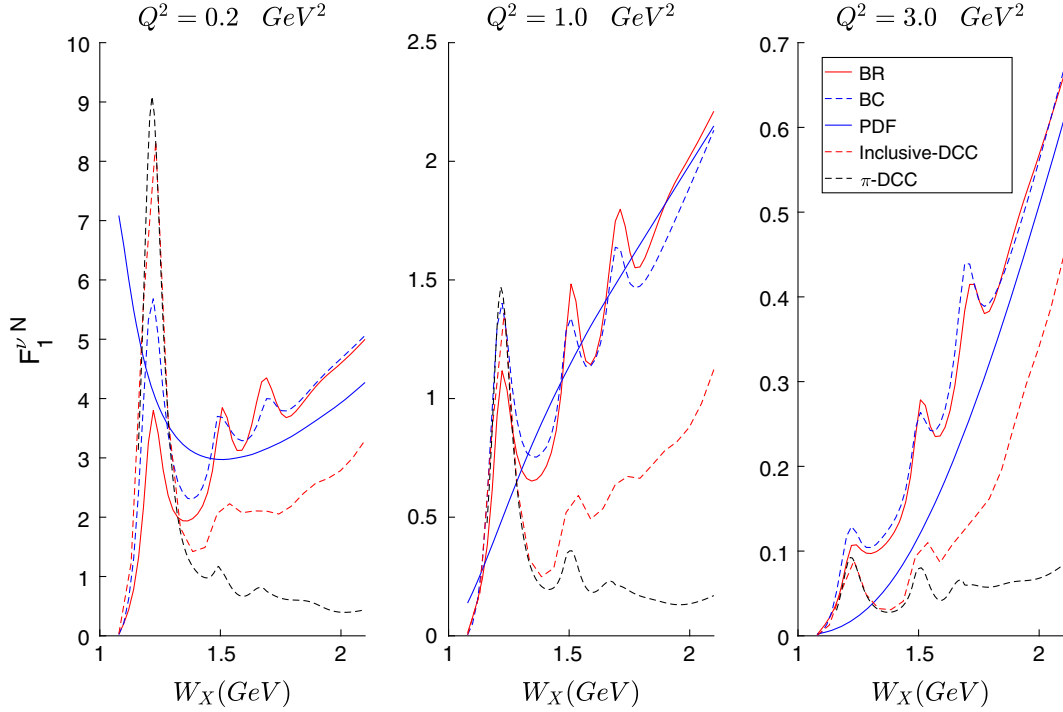


FIG. 1. Neutrino single-nucleon inelastic structure function ($F_1^{\nu N}$) versus the invariant mass (W_X) at different Q^2 values: 0.2 (left), 1.0 (center), and 3.0 (right) GeV^2 . Different prescriptions are shown, namely, Bodek-Ritchie (BR), Bosted-Christy (BC), parton distribution functions (PDF), and the π -DCC and inclusive-DCC contributions from the dynamical coupled channels (DCC) model.

For completeness, and as shown in previous works [72], the form factors employed for the QE regime are based on the Gari-Krümpelmann vector dominance model (GKex) developed in [73–75]. The form factors used to describe the 2p2h channel and their associated coupling vertices are those defined in [60].

In the following section, we compare the results obtained for electron and neutrino reactions using the SuSAv2-inelastic nuclear model together with the different approaches considered to describe the nucleon dynamics.

III. RESULTS

The description of the electron and neutrino inclusive scattering processes requires taking into account the contribution of different reaction channels. These contributions,

with their corresponding acronyms as stated in the legends, are shown in Table I as well as the model used to describe them. At low values of transferred energy ($\omega \approx Q^2/2m_N$), the dominant process is quasielastic, and it is described by the SuSAv2 superscaling model. As the value of ω increases, a process can occur in which the 2p2h states are excited via meson exchange. This is described by using the relativistic Fermi gas as a framework (RFG-MEC). At higher values of ω , we observe a series of resonances that are modeled by the SuSAv2-DCC discussed in Sec. II. In the same region, it is possible that the neutrino/electron interacts with the partons (SoftDIS), which is taken into account by a combination of SuSAv2-DCC and SuSAv2 inelastic. At even higher energy transfers, the deep inelastic scattering interactions are described by the SuSAv2-inelastic model (TrueDIS).

TABLE I. Channels that contribute to the reaction mechanism with the notation followed in the text and the model used to evaluate the cross section.

Acronym	Contribution	Model
QE	Quasielastic	SuSAv2 QE
MEC	2p2h excitations	RFG-MEC
RES	Resonances	SuSAv2-DCC
SoftDIS	Deep inelastic scattering ($W_X < 2.1 \text{ GeV}$)	SuSAv2 inelastic – SuSAv2-DCC
TrueDIS	Deep inelastic scattering ($W_X > 2.1 \text{ GeV}$)	SuSAv2 inelastic
All Contr.	All contributions	

In Sec III A, we show our predictions for double-differential inclusive electron-carbon cross sections separated in different contributions and compared with experimental data. Subsequently, in Sec III B, different neutrino-carbon/argon inclusive cross sections are shown and compared with experimental data from T2K, MINERvA, MicroBooNE, and ArgoNEUT.

A. Electron scattering

In this section, we test the models with inclusive (e, e') scattering data. The double differential electron-carbon cross section versus the energy transfer, ω , is shown in Fig. 2. In the top panels ($E = 560\text{--}1650$ MeV), we observe at lower transferred energy a peak dominated by the quasielastic contribution that is well reproduced by the SUSAv2-QE model. At higher ω , one enters into the dip region where two-particle two-hole meson exchange current contributions are needed. The second peak observed corresponds to the excitation of a Δ -resonance. In this region, the contribution provided by SuSAv2-DCC and SuSAv2-SoftDIS is in good agreement with data. In the two bottom panels ($E = 4045$ MeV, $\theta = 45^\circ, 55^\circ$), the largest contribution corresponds to SoftDIS. As shown, TrueDIS is negligible in all cases with the exception

of a minor increase observed at $\omega > 3$ GeV in the right-bottom panel. This is consistent with the quite low values of the transfer energy considered. Notice that TrueDIS is only relevant at very high ω values. Similar comments apply to the RES contribution in these panels as the Q^2 and W_X values are in general beyond the limits of the DCC model.

It is also worth mentioning a similar analysis carried out in [41], where the DCC model is implemented within the extended factorization scheme. Although the magnitude of this contribution is similar to the one presented in this work, the position of the RES peak in [41] is shifted to higher ω values, resulting in a worse agreement with data. The difference between both analyses is mainly due to the functions employed to describe the nuclear dynamics, namely the spectral functions used in the factorization scheme and the RMF-based scaling functions employed in the SuSAv2-DCC model, which mostly define the position of the peak. Furthermore, our present analysis, based on the inclusive-DCC model, incorporates additional channels to the π -DCC considered in the factorization scheme. Notice however, that the differences between both analyses are very small at the kinematics considered. Finally, also note that the SoftDIS and TrueDIS contributions included in our

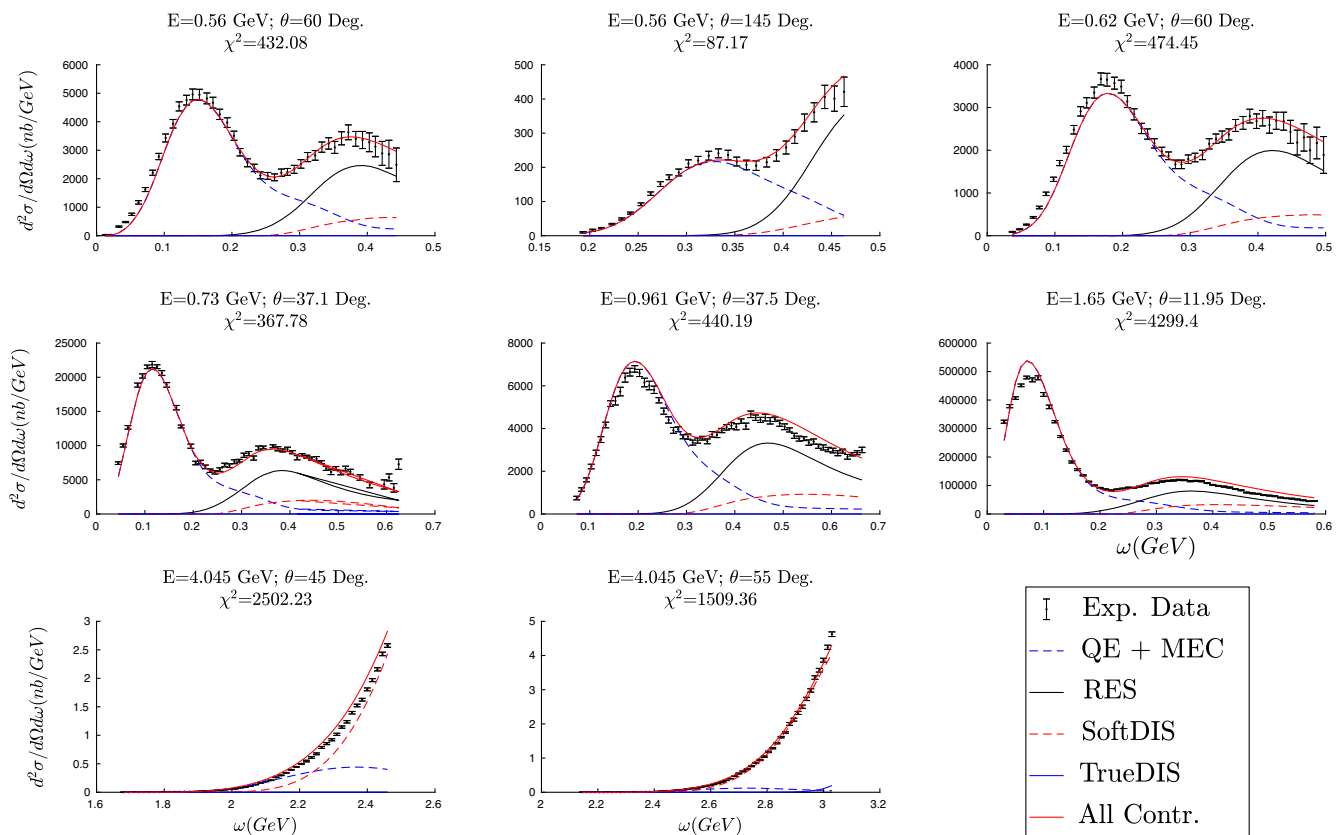


FIG. 2. Double-differential inclusive cross section for (e, e') scattering on ^{12}C at given energies and scattering angles (labeled in the panels). It is displayed in function of the transferred energy. The legend explained in Table I. Data are taken from [76]. Equation (6) has been used to obtain the results shown in the panels.

study have a rather modest impact at the kinematics analyzed, not shifting the position of the peak.

To assess the accuracy of the predictions for the double differential cross sections, for each dataset, we perform a χ^2 analysis making use of the measured covariance matrix. This matrix measures the correlations between different bins of data. The χ^2 -values are obtained as follows:

$$\chi_{i,j}^2 = (x_{i,\text{measured}} - x_{i,\text{expected}}) V_{ij}^{-1} (x_{j,\text{measured}} - x_{j,\text{expected}}) \quad (4)$$

$$\chi^2 = \sum_i \sum_j \chi_{i,j}^2, \quad (5)$$

where the indices i, j denote a given pair of data bins, x_{measured} is the cross section measured in the experiments, x_{expected} is the cross section predicted by the models, and V is the measured covariance matrix provided by the experiments. In the analysis for neutrinos shown in the next section, we provide, for each set of data, both the value of $\chi_{i,j}^2$ for each data bin (4) and the sum of all the χ^2 values (5). In those cases where the covariance matrix is not provided by the released data (single-differential cross sections), the χ^2 analysis is performed using the following expression:

$$\chi^2 = \sum_i \left(\frac{x_{i,\text{expected}} - x_{i,\text{measured}}}{\Delta x_{i,\text{measured}}} \right)^2, \quad (6)$$

where $\Delta x_{i,\text{measured}}$ is the uncertainty associated to the measurements. We specify in the analysis that follows which specific χ^2 expression is used. In the case of electron scattering data we observe that the values of χ^2 are very sensitive due to the small data error bars leading to very large χ^2 -values in some cases. We have checked that removing some of the lower ω data in the fourth panel of Fig. 2, the χ^2 -values obtained can differ by a factor ~ 8 .

Summarizing, we have shown that the different models considered in this work are capable to provide a precise description of electron scattering data. Thus, in what follows, we apply these models to the case of neutrino scattering processes.

B. Neutrino scattering

In next sections, we show our theoretical predictions and compare them with CC inclusive neutrino scattering data corresponding to different experiments. We also provide in all cases the χ^2 -analysis.

1. T2K

In the T2K experiment, the target used consists of a mixture of carbon (86.1%), hydrogen (7.4%), and oxygen (3.7%) [6], and the neutrino flux peaks at ~ 0.6 GeV. In Fig. 3, the CC inclusive ν_μ -CH double differential cross section per nucleon is displayed for various angular bins as

a function of the muon momentum p_μ . In what follows, we assume a pure CH target for our calculations, neglecting the effect of the small amount of oxygen in the experimental target that can be considered equivalent to carbon. The effects of other nuclei, apart from C and H, in the theoretical calculations will be addressed in further works. In the case of the resonance and DIS channels, we also take into account the contribution of hydrogen in the CC ν_μ -H reaction, which does not contribute to the QE and 2p2h channels. In general, this contribution is very minor at T2K kinematics, almost negligible, particularly at very backwards angles. In the opposite case, *i.e.*, very forward angles, the effect is less than a 5% increase in the RES and DIS channels. On the contrary, more relevant contributions are observed at MINERvA ME kinematics (see Sec. III B 2 for details), where the enhancement of the inelastic cross section due to the H contribution is of the order of $\sim 50\%$ ($\sim 25\%$) for the p_T bin of $0 < p_T < 0.07$ GeV/c ($0.07 < p_T < 0.15$ GeV/c) and is dominated by the RES channel.

In each panel of Fig. 3, two sets of data are shown, corresponding to experimental analyses performed using the GENIE [77] and NEUT [78,79] generators. The theoretical predictions for the cross section are folded with the T2K flux and the different channels are shown separately. In general, the sum of QE and MEC processes gives about 40% of the cross section and provides the biggest contribution. The resonance contribution varies between roughly 20% and 35% and decreases as the scattering angle gets larger. TrueDIS and SoftDIS are not very important above $\sim 30^\circ$ of scattering angle. However, at lower angles and for muon momentum above 1.5 GeV, these contributions become crucial in order to reproduce the data, being TrueDIS the most important one in most of the situations. Only at the higher p_μ data in the last panel, the SoftDIS contribution becomes relevant. As shown, at values of the momentum below 1.5 GeV, some data points are overestimated. This excess can be fixed by using relativistic mean field (RMF) or energy dependent relativistic mean field (ED-RMF) models [23,80], as it is confirmed in Fig. 4 for the last three angular bins. A similar correction can also be observed in [81], where at low momentum the quasi-elastic contribution is reduced via the random phase approximation. Note also that the above-mentioned analysis tends to underestimate the data at muon momentum higher than 1.5 GeV as DIS contributions and other resonances apart from the ones related to pion production are not included. The results are rather similar to the ones found in our previous work [42], where the SuSAv2-inelastic model was used. Moreover, the χ^2 -values are also very close to the ones presented in the simulations with GENIE and NEUT [6].

In Fig. 5, we compare our prediction for the total electron neutrino and antineutrino cross section on hydrocarbon

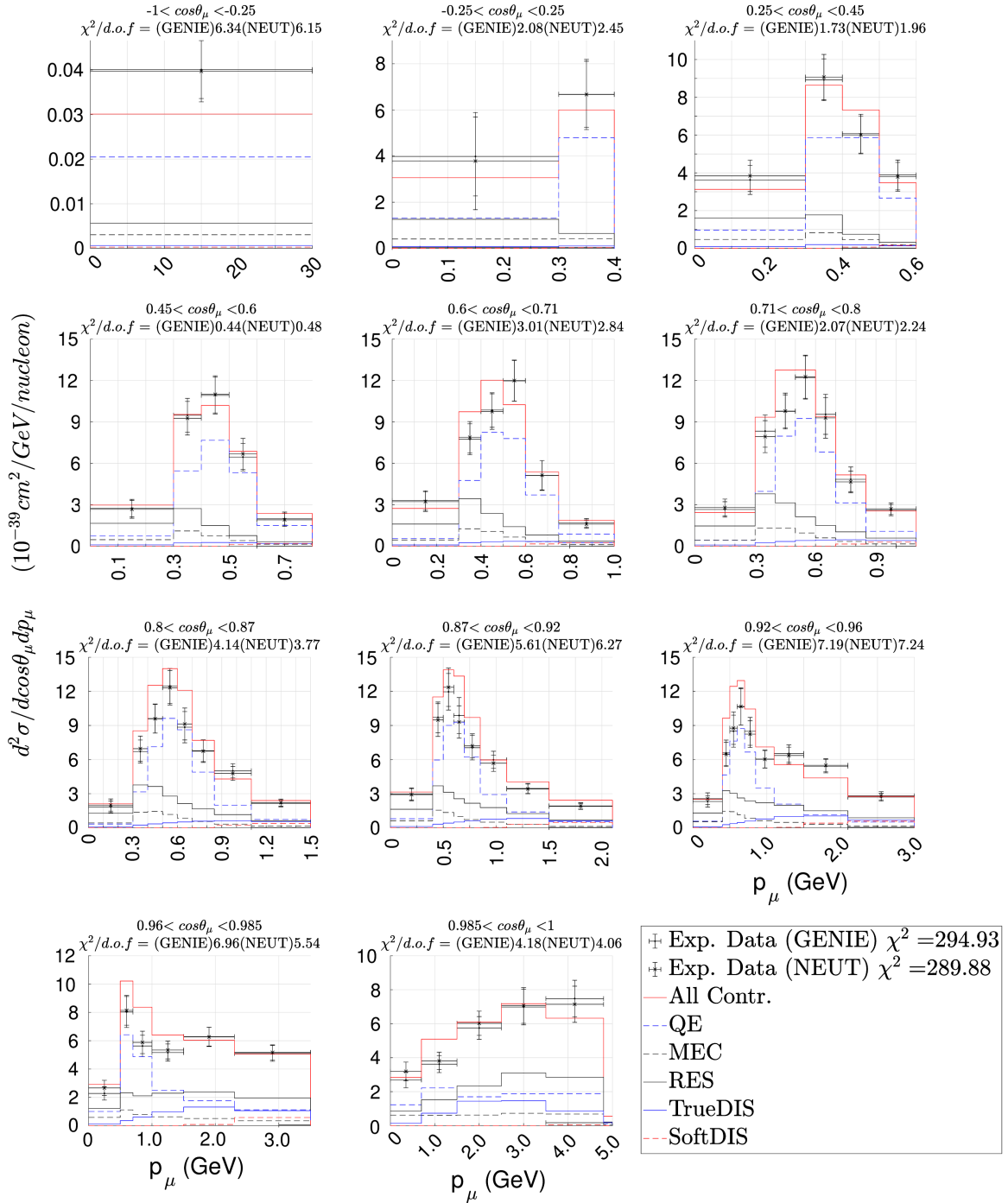


FIG. 3. T2K CC inclusive flux-averaged double-differential cross section on CH per target nucleon in bins of the muon scattering angle (labeled in panels) as function of the muon momentum. The different contributions are shown individually. Also, we show the sum of all of them (see Table I). Data are taken from [6]. The χ^2 -value shown in each panel is a partial calculation associated to each bin. We are using Eq. (5) to calculate the result portrait in the legend.

against the electron momentum p_e with data corresponding to forward (FHC) and reversal (RHC) horn current flux. The FHC electron neutrino flux peaks at ~ 1.2 GeV, whereas the RHC (anti)neutrino flux peaks at $\sim (0.85)1.95$ GeV. As observed, the data below

$p_e = 3$ GeV match our predictions whereas at higher electron momentum our models clearly underestimate data for most kinematics. The values of χ^2 corresponding to NEUT and GENIE data are very similar and slightly smaller than the ones given in [7].

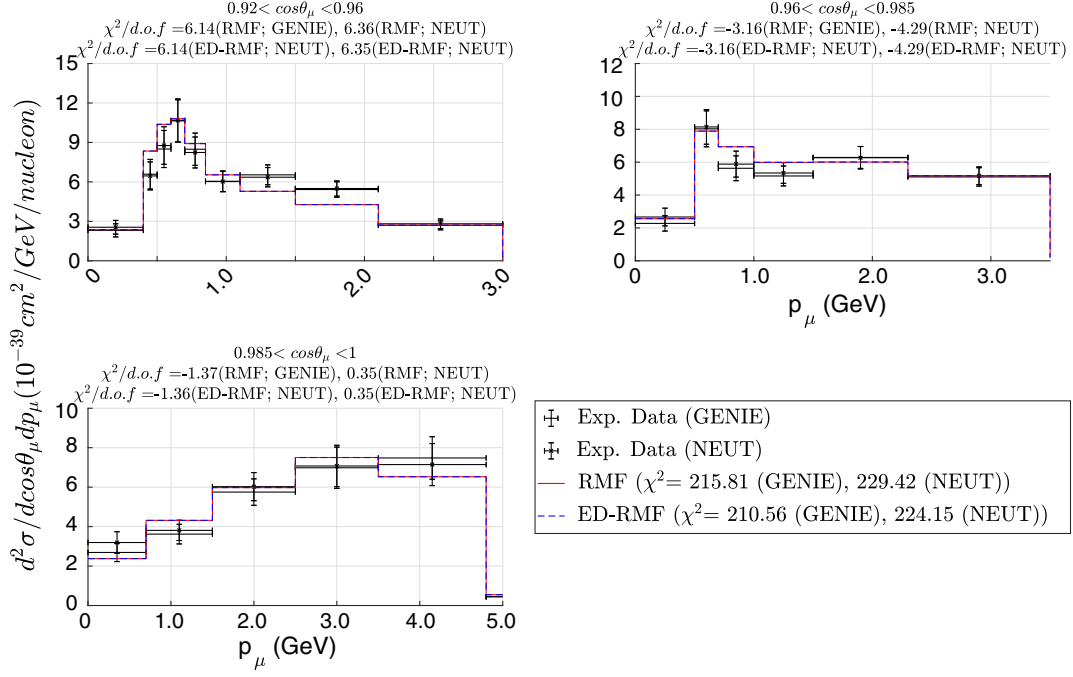


FIG. 4. T2K CC inclusive flux-averaged double-differential cross section on CH per target nucleon in bins of the muon scattering angle (labeled in panels) as function of the muon momentum. Unlike Fig. 3, QE contributions have been obtained using RMF and ED-RMF models, respectively. Theoretical curves show the total contribution (QE + MEC + RES + SoftDIS + TrueDIS). Data are taken from [6].

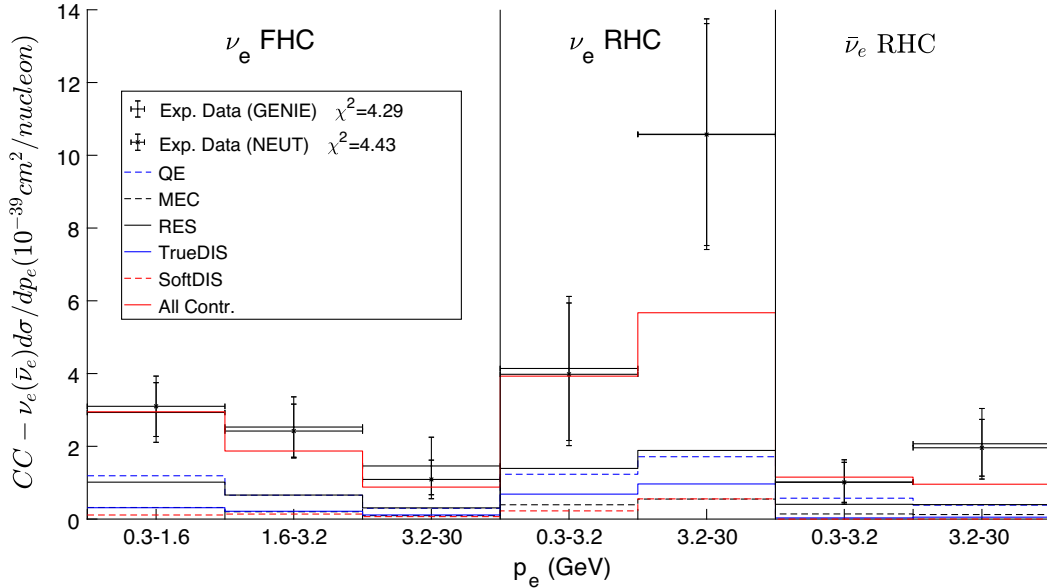


FIG. 5. T2K CC electron neutrino and antineutrino inclusive flux-averaged total cross section on CH per target nucleon as function of the electron momentum. Different fluxes are used: forward horn current (FHC) and reversal horn current (RHC). The legend is as in previous figures (see Table I). Data are taken from [7].

2. MINERvA

In this section, we analyze the double and single differential flux-folded ν_μ -CH inclusive cross sections per target nucleon versus the longitudinal ($p_L \equiv p_\mu \cos \theta_\mu$) and transverse ($p_T \equiv p_\mu \sin \theta_\mu$) momentum of the muon.

The target for the MINERvA experiment is a mixture of carbon (88.5%), hydrogen (8.2%), and oxygen (2.5%) [4], and the angular acceptance is limited to $\theta_\mu < 20^\circ$. As in the previous case, T2K experiment, we assume a pure CH target for our calculations and include hydrogen for the

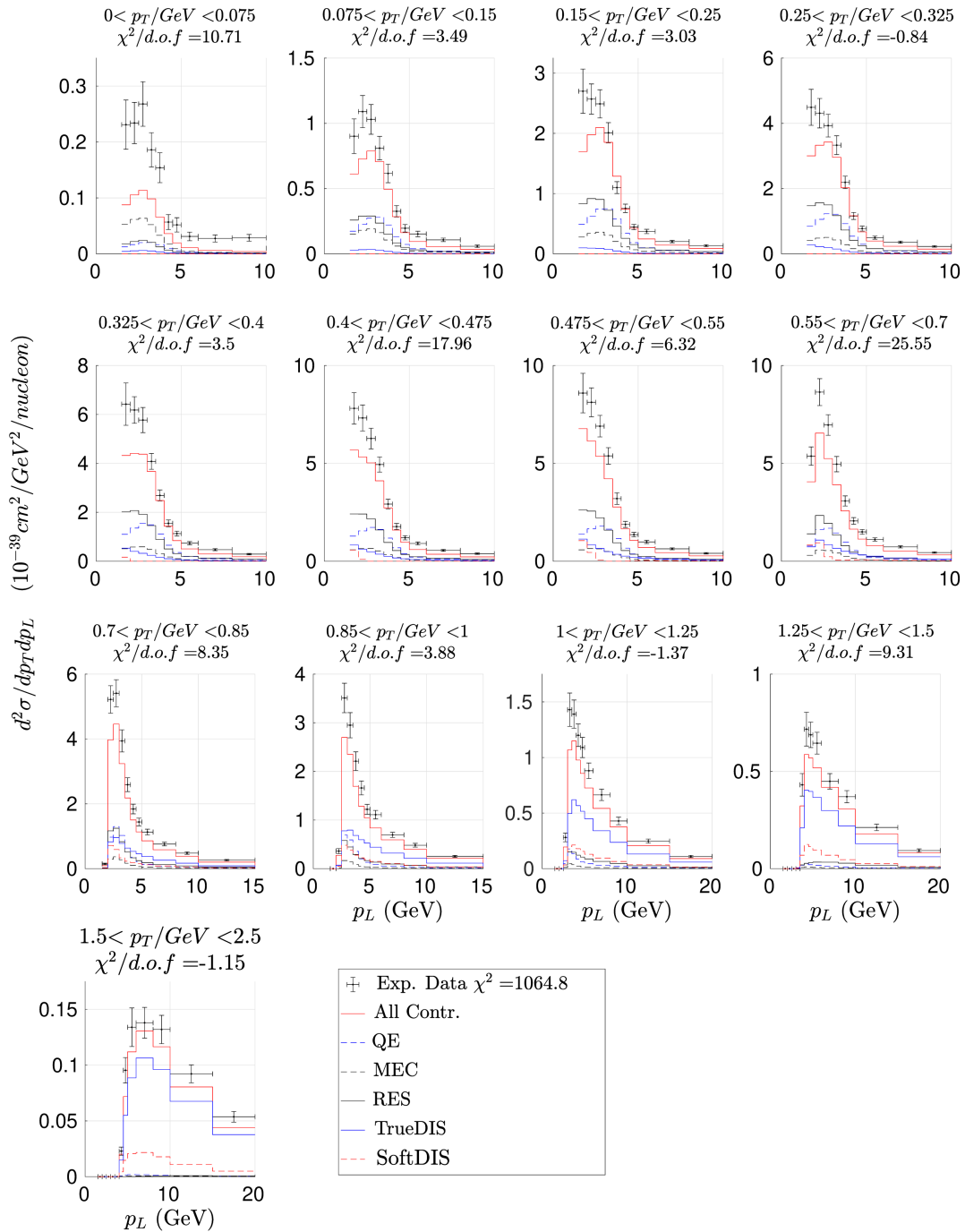


FIG. 6. MINERvA CC inclusive (LE) flux-averaged double-differential cross section on CH per target nucleon in bins of the transverse momentum as a function of the longitudinal momentum. The legend is as in previous figures (see Table I). Data are taken from [4]. The χ^2 -value shown in each panel is a partial calculation associated to each bin. We are applying Eq. (5) to calculate the results shown in the legend.

analysis of the resonance and deep inelastic scattering channels. These contributions lead to small effects at low values of the longitudinal muon momentum, being negligible at higher values. There are two sets of data corresponding to the two MINERvA fluxes, called low energy (LE) and medium energy (ME) fluxes. In the LE case, the neutrino energy flux is peaked at ~ 3.5 GeV, and the

muon momentum is limited to $1.5 < p_L/\text{GeV} < 20$, $p_T < 2.5$ GeV. In the ME case, the neutrino flux peaks at ~ 6 GeV, and the muon momentum is limited to $1.5 < p_L/\text{GeV} < 60$, $p_T < 4.5$ GeV.

In Figs. 6 and 7, the double differential cross section folded with the LE flux is presented as a function of p_L and p_T , respectively. At low p_T , QE scattering gives the largest

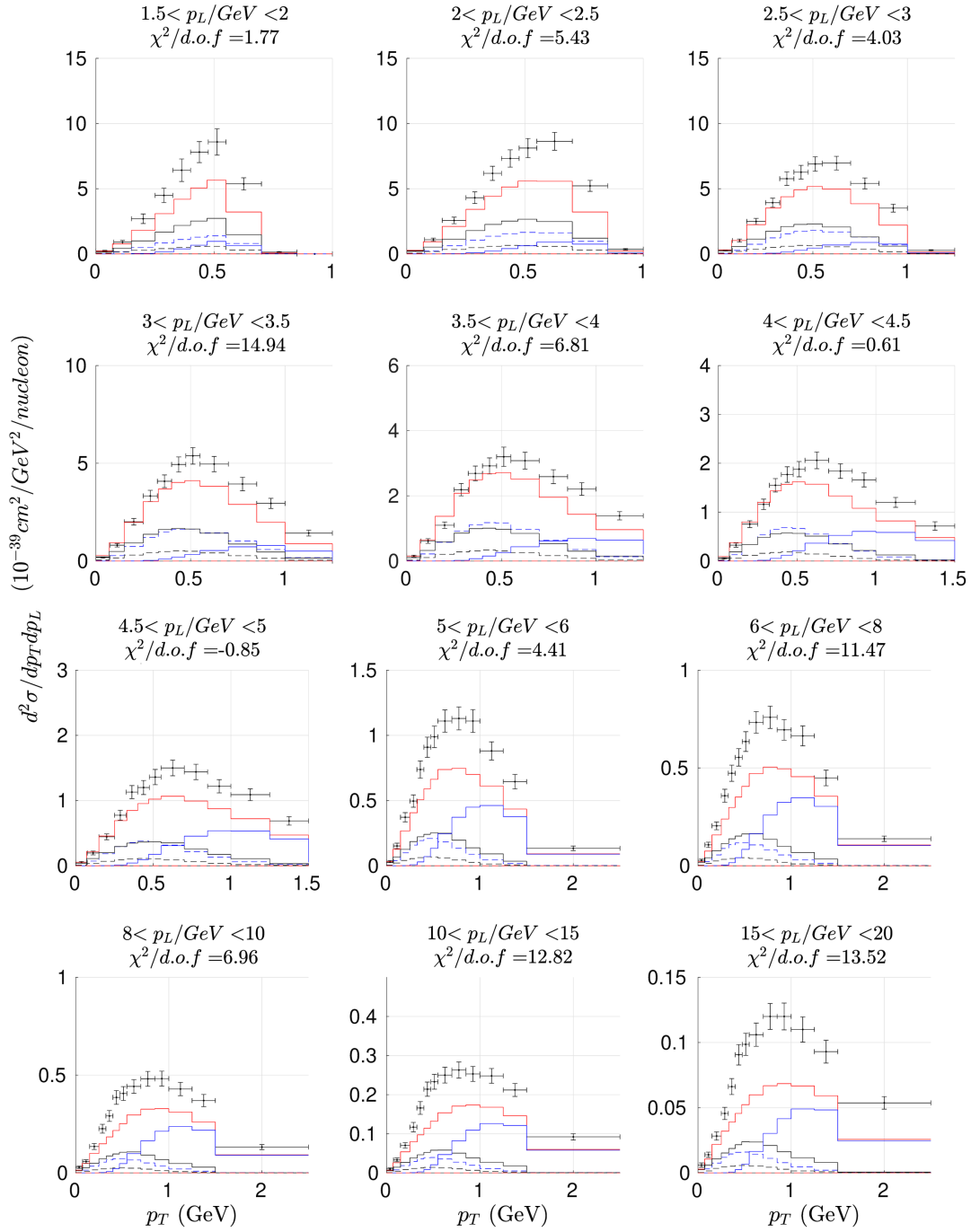


FIG. 7. MINERvA CC inclusive (LE) flux-averaged double-differential cross section on CH per target nucleon in bins of the longitudinal momentum as a function of the transverse momentum. The legend is as in previous figures (see Table I). The same legend as Fig. 6. Data are taken from [4]. The χ^2 -value shown in each panel is a partial calculation associated to each bin.

contribution to the cross section, followed by RES and MEC. As the transverse momentum increases, TrueDIS becomes more and more important, overcoming the RES contribution. Compared to MINERvA GENIE predictions [4], we lack strength in the RES contribution but get similar results for the other terms. This disagreement in the RES predictions might be connected with the nuclear effects implemented in the SuSv2 inelastic scaling

function. Another source of differences can be linked to the Rein-Sehgal pion production model used in the Monte Carlo simulations. This is an oversimplified description of the resonance contribution that cannot reproduce accurately the behavior of the cross section. This topic is discussed later. On the other hand, our χ^2 -analysis gets higher values than the ones presented by the simulations. We show the χ^2 -values divided by the number of data

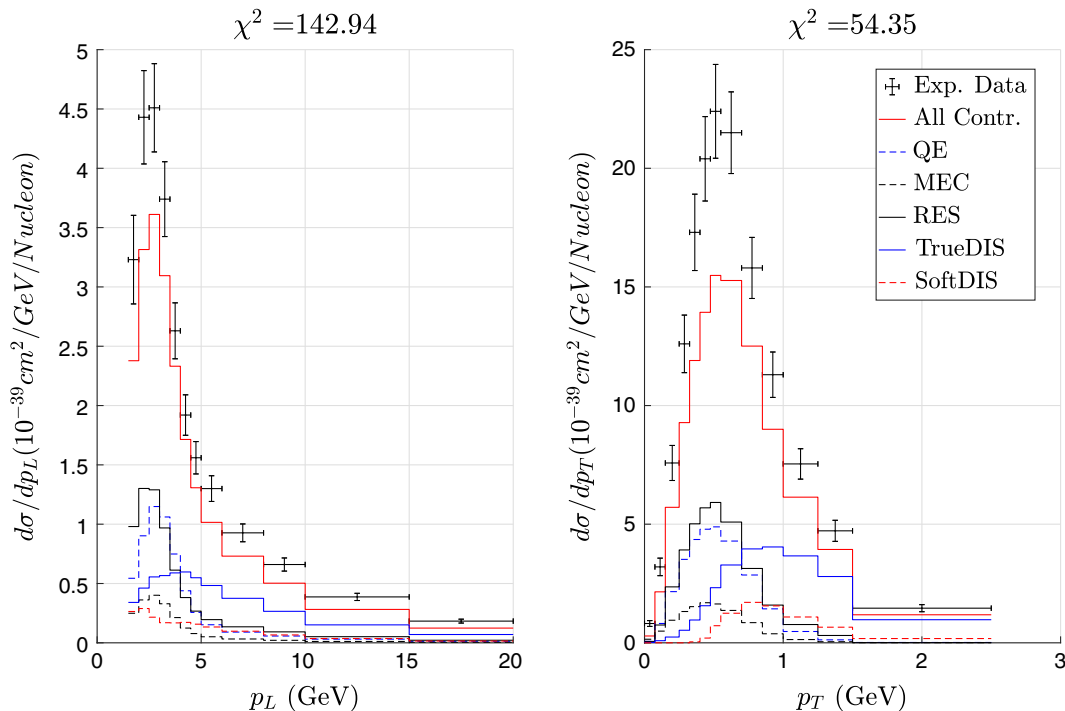


FIG. 8. MINERvA CC inclusive (LE) flux-averaged single-differential cross section on CH per target nucleon as function of the longitudinal momentum (left) and the transverse momentum (right). The legend is as in previous figures (see Table I). Data are taken from [4]. The χ^2 -values are calculated using Eq. (5).

points, so they can be compared directly for the different kinematical situations analyzed.

In Fig. 8, we show the LE single-differential cross sections versus p_L (left panel) and p_T (right). According to our prediction, QE and MEC account for around 30% of the total strength. This is similar to the contribution ascribed to the TrueDIS channel, while SoftDIS only provides about 10% of the total cross section. The SuSav2-DCC model gives around 30% of the total contribution, being of similar magnitude to the QE + MEC and TrueDIS ones. However, as in the previous case, the data are underestimated. In general, the contributions from the different channels are similar to the ones shown by MC simulations in [4], except for the resonance channel that is significantly larger in MC simulations. This explains why our model predictions are clearly below the data.

In Figs. 9 and 10, we show the double differential cross section folded by the ME flux. As observed, the results and their comparison with data are very similar to the ones for the LE flux. In this case, compared to the analysis presented in [4], we lack strength in the SoftDIS contribution, and we tend to underestimate data by $\sim 20\%$. The χ^2 -values are larger than the ones presented by the models used in MINERvA simulations and the ones shown for the LE flux.

Finally, in Fig. 11, the single-differential cross section folded by the ME flux is shown. QE and MEC contributions are around 25%, being the inelastic channels the ones that dominate at these kinematics. TrueDIS and SoftDIS

contributions provide around half of the total strength of the cross section. The resonance contribution is around a 25% of the total contribution, being similar to the QE + MEC ones. As in previous cases, our predictions clearly underestimate the data by a factor ~ 1.4 – 1.3 in the region of the maximum.

This source of discrepancy between our predictions and data analysis based on GENIE simulations is better illustrated in the results presented in Fig. 12. Here, we explore the case of reducing the nuclear effects in the resonance channel by comparing the standard SuSav2-DCC approach with a RFG model using a very low Fermi momentum ($k_F = 5$ MeV/c) for the latter. Notice that the decrease of k_F in the RFG approach produces results closer to data. It is important to point out that the RFG predictions at very small k_F -values mimic the single-nucleon prediction; *i.e.*, nuclear effects are dismissed. Hence, the discrepancy between our two models in Fig. 12 is clearly connected with the nuclear effects introduced within the SuSav2 approach. The magnitude of these RFG results are consistent with the resonance model implemented in MINERvA GENIE [77], that is based on a single-nucleon Rein-Sehgal pion production model with lepton mass corrections. The GENIE approach increases the original Rein-Sehgal RES contribution by $\sim 20\%$ – 40% , that seems to coincide with the discrepancies observed in Fig. 12. However, further studies are needed to clarify this issue.

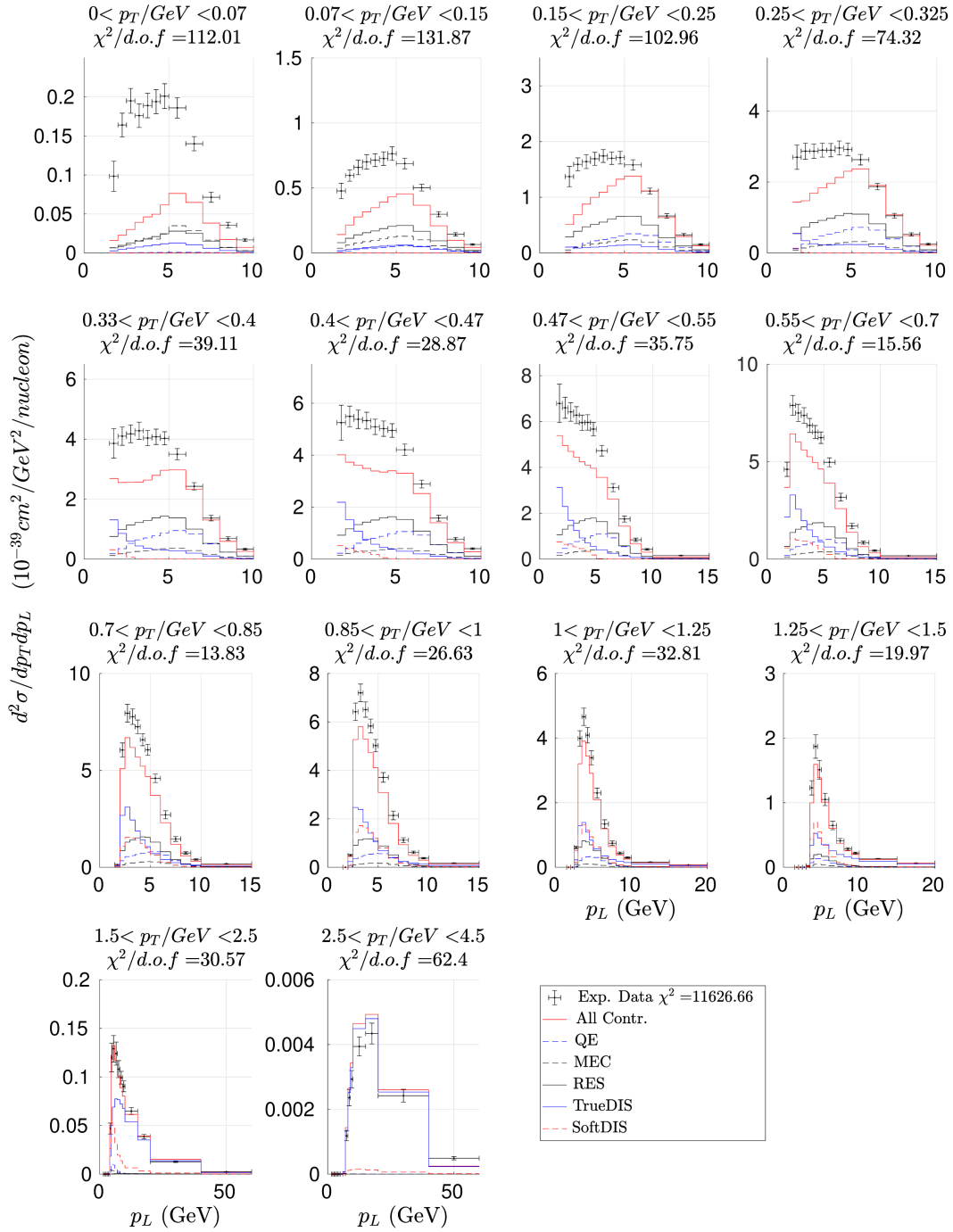


FIG. 9. MINERvA CC inclusive (ME) flux-averaged double-differential cross section on CH per target nucleon in bins of the transverse momentum as function of the longitudinal momentum. The legend is as in previous figures (see Table I). Data are taken from [5]. The χ^2 -value shown in each panel is a partial calculation associated to each bin. We are using Eq. (5) to calculate the result portrait in legend.

3. MicroBooNE

The MicroBooNE neutrino beam flux is peaked at ~ 0.8 GeV, and the target is liquid argon. In Fig. 13, we show the CC-inclusive ν_μ - ^{40}Ar double differential cross section versus the muon momentum for different scattering angle bins. In each case, we also present the χ^2 analysis. As

observed, the discussion of the results follows similar trends to the ones applied to T2K. On one hand, QE plus MEC contributions dominate at all kinematics, being around 70% of the cross section. On the other, the RES contribution provides around 20%–30% of the total strength, and it increases as the scattering angle gets smaller. Finally, TrueDIS and SoftDIS contributions are not very relevant

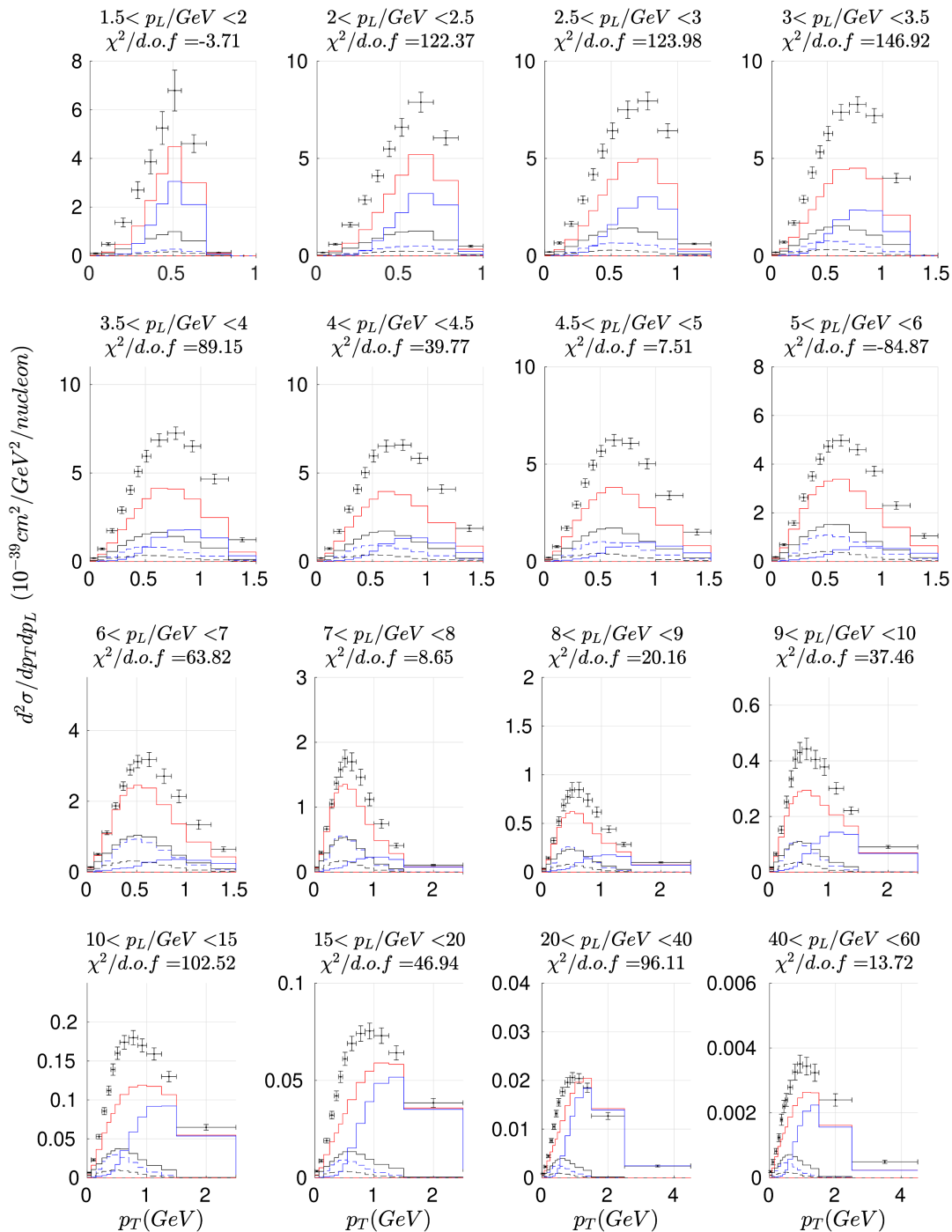


FIG. 10. MINERvA CC inclusive (ME) flux-averaged double-differential cross section on CH per target nucleon in bins of the longitudinal momentum as function of the transverse momentum. The legend as in previous figures (see Table I). The same legend as Fig. 9 taken from [5]. The χ^2 -value shown in each panel is a partial calculation associated to each bin.

for these kinematics, being below 6% of the cross section in all cases. Furthermore, there is a shift between our prediction and the experimental data at very backward angles; for instance, the cross section peaks at lower muon momentum than the data, and the opposite is observed at very forward angles. In general, our models provide a rather good

description of the data, except at the lowest scattering angles, where the predicted shift is too strong. This shift is also present in other analyses like the ones shown in [81], which in general present a similar behavior to our results. Finally, we should note that the GENIE χ^2 results are smaller than the ones obtained in our analysis.

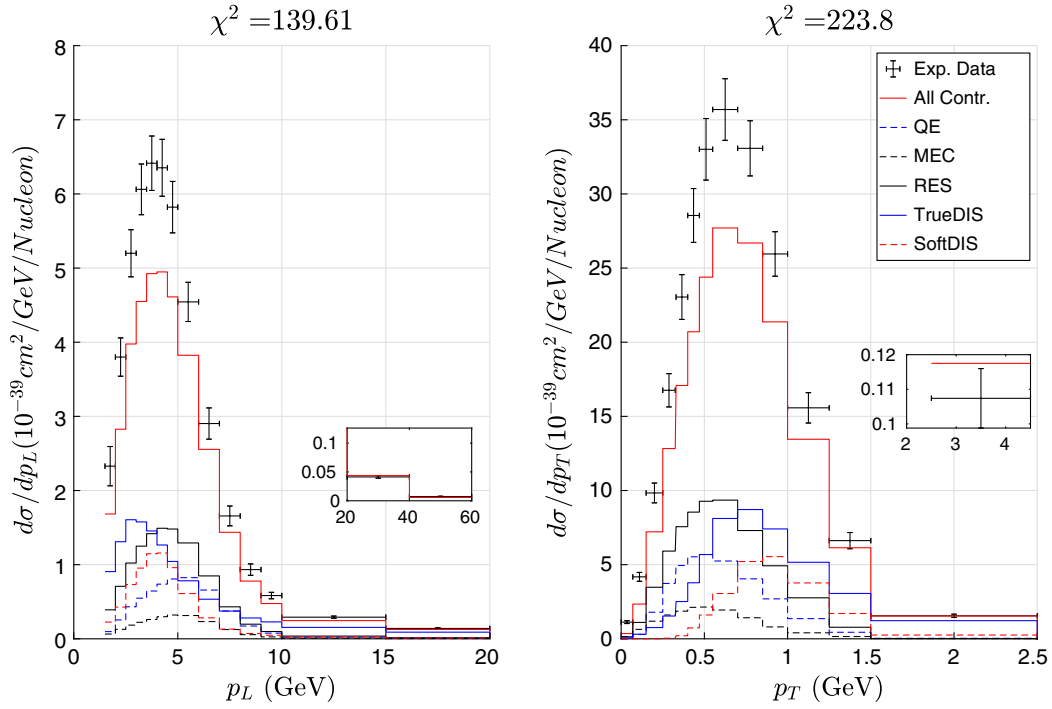


FIG. 11. MINERvA CC inclusive (ME) flux-averaged single-differential cross section on CH per target nucleon as function of the longitudinal momentum (left) and the transversal momentum (right). Legend as in previous figures (see Table I). Data are taken from [5]. The χ^2 -values are calculated using Eq. (6).

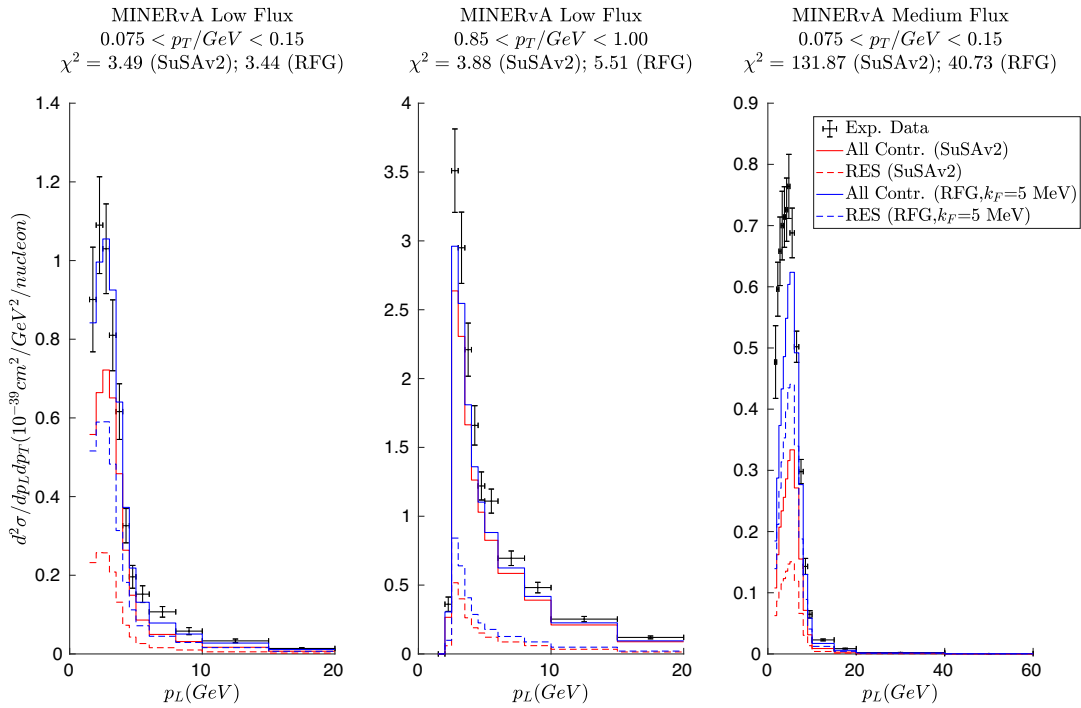


FIG. 12. MINERvA CC inclusive (LE and ME) flux-averaged double-differential cross section on CH per target nucleon as function of the longitudinal momentum. Dashed lines represent the resonance (RES) contribution, and the continuous line is related to the sum of all the contributions (All Contr.). Red (blue) lines represent the results using SuSAv2-DCC (RFG with $k_F = 5$ MeV/c) for the RES channel. χ^2 values are shown for the two cases. Data are taken from [5].

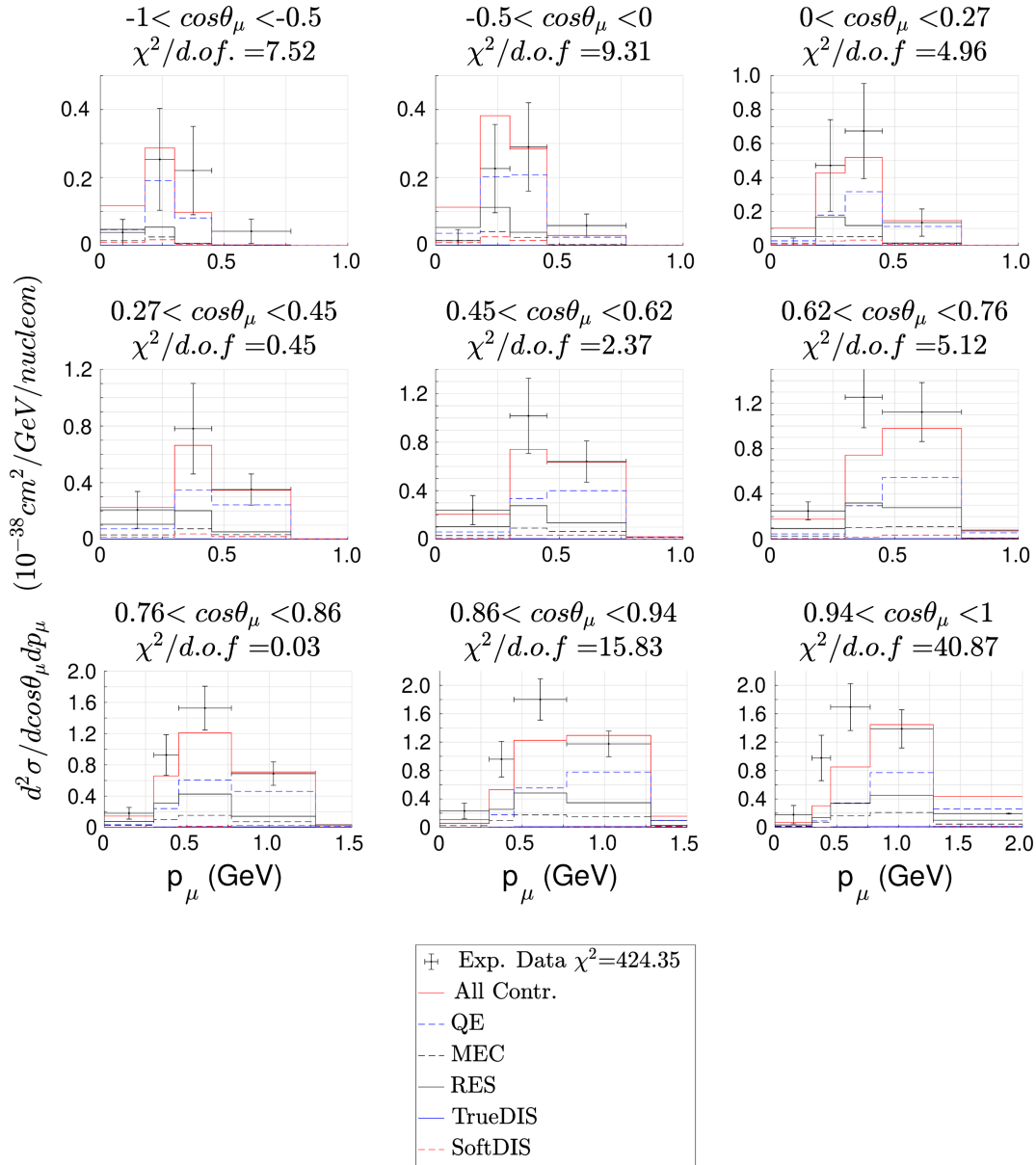


FIG. 13. MicroBooNE CC inclusive flux-averaged double-differential cross section on Ar per target nucleon in bins of the muon scattering angle as function of the muon momentum. The legend is as in previous figures (see Table I). Data are taken from [2]. The χ^2 -value shown in each panel is a partial calculation associated to each bin. We are using Eq. (5) to calculate the result portrait in legend.

4. ArgoNEUT

In the ArgoNEUT experiment, as for MicroBooNE, the target is liquid argon. The ArgoNEUT(2012) neutrino flux peaks at 4.5 GeV. The (anti)neutrino ArgoNEUT(2014) flux is peaked at (3.6) 9.6 GeV. In Figs. 14 and 15, the CC-inclusive ν_μ - ^{40}Ar flux-folded single differential cross section is shown as a function of the muon momentum p_μ (left panel in Fig. 14 and top panels in Fig. 15) and the scattering angle θ_μ (right panel in Fig. 14, bottom panels in Fig. 15). The acceptance is $\theta_\mu < 36^\circ$, and the muon momentum is limited to $p_\mu < 25$ GeV. For neutrinos (Fig. 14 and left panels in Fig. 15), it is observed that

QE, MEC and RES provide $\sim 50\%$ of the strength of the cross section for ArgoNEUT (2012). Meanwhile, for ArgoNEUT (2014), TrueDIS is the dominant contribution by giving $\sim 65\%$ of the strength of the cross section. Notice that our predictions underestimate data, particularly in the region where the cross section reaches its maximum. Nevertheless, the models are capable of explaining the fall of the cross section.

In the case of antineutrinos (right panels in Fig. 15), the models reproduce the cross section data reasonably well. It is worth noticing that the flux is different for antineutrinos and neutrinos, peaking at different energies. In the case of antineutrinos, QE plus MEC provides $\sim 40\%$ of the total

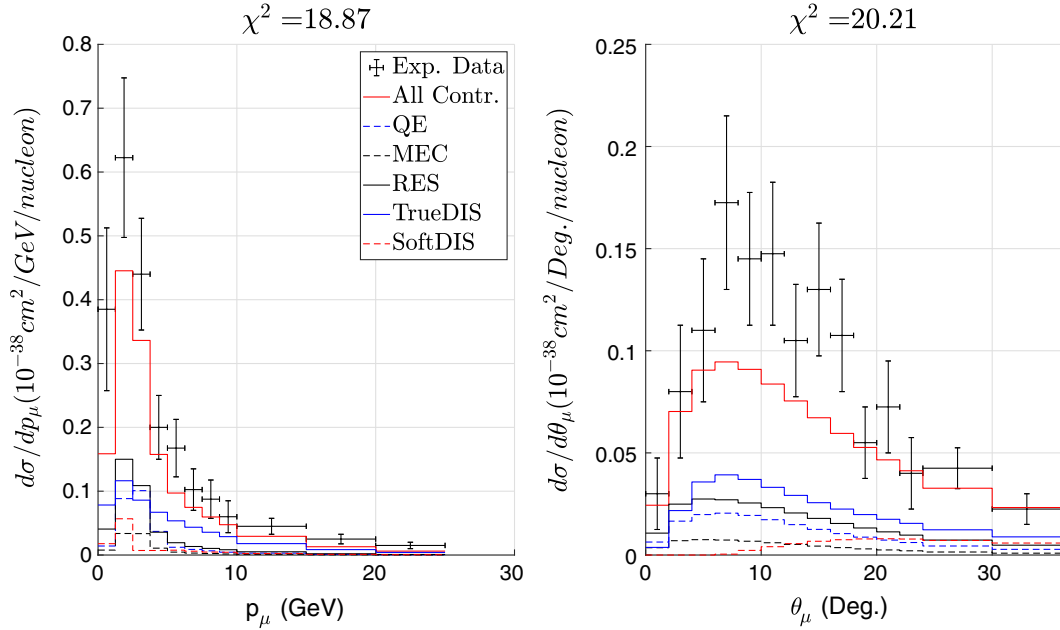


FIG. 14. Argonne (2012) CC inclusive flux-averaged single-differential neutrino cross section on Ar per target nucleon as function of the muon momentum (left) and as a function of the scattering angle (right). The legend is as in previous figures (see Table I). Data are taken from [11]. The χ^2 -values are calculated using Eq. (6).

strength, whereas the inelastic channels are dominated by the RES contribution. This is clearly in contrast to the results observed for neutrinos, and it is linked to the nice accordance between our theoretical predictions and data for antineutrinos, whereas they depart significantly in the case of neutrinos. However, further studies are needed to explain which basic ingredients in the analysis of Argonne (anti)neutrino-nucleus scattering are responsible of the differences observed in both cases.

IV. CONCLUSIONS

In this work, we have expanded upon the SuSAv2-inelastic model, presented in previous work [42], by implementing the dynamical coupled channels model [38], which takes into account all the possible resonances of the nucleon and their mutual interactions involving pions, double pions, kaons, etc. This represents a clear improvement of the previous model, in which the resonance region was described by phenomenological fits. However the limitation of the DCC model to resonance production makes it necessary to add the deep inelastic scattering contribution that may occur in the same kinematic region: this we do by using the original SuSAv2-inelastic model with appropriate kinematic cuts. The two models complement each other to obtain what we define as SoftDIS contribution. The rest of the inelastic spectrum is described by the SuSAv2-inelastic model alone.

This new iteration of the model has been tested against electron-carbon scattering data with excellent results in a wide range of kinematics. After that, the model has been

applied to neutrino scattering, and compared its predictions with several CC-inclusive data.

For T2K and MicroBooNE, the model is capable to explain the data really well. The discrepancies between predictions and data from these experiments are very similar to those found in our previous work [42] and, particularly in the case of T2K, they are not related to the resonance contribution.

In the case of MINERvA and Argonne, which operate at higher energies, our results tend to underestimate the experimental data. In general, for the low energy MINERvA flux, the resonance contribution lacks the strength shown by Monte Carlo simulations [4], while SoftDIS lacks strength for the medium energy MINERvA flux. In the results for neutrinos from Argonne, we also lack strength in general in comparison with data. However, the antineutrino Argonne data, corresponding to lower energy, are well explained by the model.

In comparing with experimental data, we have performed a χ^2 analysis in order to quantify the quality of the agreement and compare it with the one reported in the experimental papers and obtained by the Monte Carlo simulations. We have found that, in general, the SuSAv2 model gives larger values of χ^2 than those obtained by the simulations. These discrepancies need further investigation. However, it should be stressed that our model does not contain any free parameter: the few parameters have been fixed once and for all by comparing with electron scattering data [43]. Therefore, no “tuning” of the model is performed to adjust to neutrino data.

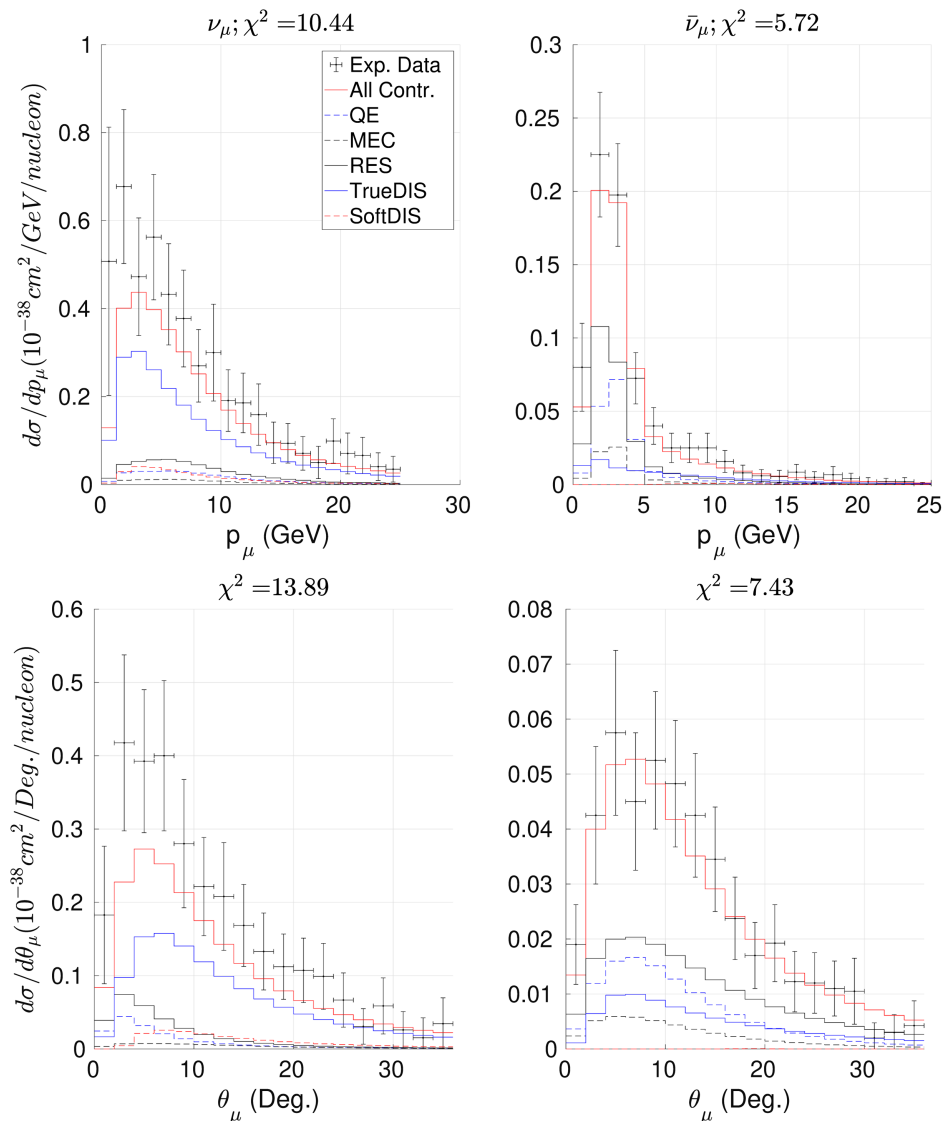


FIG. 15. ArgoNEUT (2014) CC inclusive flux-averaged single-differential cross section on Ar per target nucleon as function of the muon momentum (top) for neutrinos (left) and antineutrinos (right) and as a function of the scattering angle (bottom). The legend as in previous figures (see Table I). Data are taken from [8]. The χ^2 -values are calculated using Eq. (6).

In future works, we plan to implement other resonance models [36] in the SuSAv2 framework. Moreover, the recent inclusion of the DCC model in the NEUT simulator will allow for a direct comparison with our predictions.

ACKNOWLEDGMENTS

This work was partially supported by the Spanish Ministerio de Ciencia, Innovación y Universidades and ERDF (European Regional Development Fund) under Contract No. PID2020-114687 GB-100, by the Junta de Andalucía (Grants No. FQM160, No. SOMM17/6105/

UGR/UGR, and No. P20-01247), by University of Tokyo ICRR's Inter-University Research Program FY2022 (Ref. No. 2022i-J-001) and FY2023 (Ref. No. 2023i-J-001), by the INFN under Project Iniziativa Specifica NucSys and the University of Turin under Project No. BARM-RILO-20 (M. B. B.). J. G. R. was supported by a Contract No. PIF VI-PPITUS 2020 from the University of Seville (Plan Propio de Investigación y Transferencia) associated with the Project No. PID2020-114687 GB-100. J. M. F.-P. acknowledges support from a fellowship from the Ministerio de Ciencia, Innovación y Universidades. Programa FPI (Spain).

- [1] L. Alvarez-Ruso *et al.*, *Prog. Part. Nucl. Phys.* **100**, 1 (2018).
- [2] P. Abratenko *et al.* (MicroBooNE Collaboration), *Phys. Rev. Lett.* **123**, 131801 (2019).
- [3] M. A. Acero *et al.* (NOvA Collaboration), *Phys. Rev. Lett.* **130**, 051802 (2023).
- [4] A. Filkins *et al.* (MINERvA Collaboration), *Phys. Rev. D* **101**, 112007 (2020).
- [5] D. Ruterbories *et al.* (MINERvA Collaboration), *Phys. Rev. D* **104**, 092007 (2021).
- [6] K. Abe *et al.* (T2K Collaboration), *Phys. Rev. D* **98**, 012004 (2018).
- [7] K. Abe *et al.* (T2K Collaboration), *J. High Energy Phys.* **10** (2020) 114.
- [8] R. Acciarri *et al.* (The ArgoNeuT Collaboration), *Phys. Rev. D* **89**, 112003 (2014).
- [9] Aguilar-Arevalo *et al.* (MiniBooNE Collaboration), *Phys. Rev. D* **81**, 092005 (2010).
- [10] R. Acciarri *et al.* (DUNE Collaboration), arXiv:1512.06148.
- [11] C. Anderson *et al.* (ArgoNeuT Collaboration), *Phys. Rev. Lett.* **108**, 161802 (2012).
- [12] K. Abe *et al.* (Hyper-Kamiokande Proto-Collaboration), arXiv:1805.04163.
- [13] M. B. Barbaro, J. A. Caballero, T. W. Donnelly, and C. Maieron, *Phys. Rev. C* **69**, 035502 (2004).
- [14] J. E. Amaro, M. B. Barbaro, J. A. Caballero, T. W. Donnelly, A. Molinari, and I. Sick, *Phys. Rev. C* **71**, 015501 (2005).
- [15] T. Sato and T.-S. H. Lee, *J. Phys. G* **36**, 073001 (2009).
- [16] K. Joo *et al.* (CLAS Collaboration), *Phys. Rev. C* **68**, 032201 (2003).
- [17] K. Abe *et al.* (T2K Collaboration), *Phys. Rev. D* **95**, 012010 (2017).
- [18] O. Lalakulich, E. A. Paschos, and G. Piranishvili, *Phys. Rev. D* **74**, 014009 (2006).
- [19] E. Vagnoni, O. Benhar, and D. Meloni, *Phys. Rev. Lett.* **118**, 142502 (2017).
- [20] R. González-Jiménez, K. Niewczas, and N. Jachowicz, *Phys. Rev. D* **97**, 013004 (2018).
- [21] T. Katori and M. Martini, *J. Phys. G* **45**, 013001 (2018).
- [22] M. Sajjad Athar and J. G. Morfin, *J. Phys. G* **48**, 034001 (2021).
- [23] R. González-Jiménez, A. Nikolakopoulos, N. Jachowicz, and J. M. Udías, *Phys. Rev. C* **100**, 045501 (2019).
- [24] M. Martini, M. Ericson, G. Chanfray, and J. Marteau, *Phys. Rev. C* **80**, 065501 (2009).
- [25] M. V. Ivanov, J. M. Udías, A. N. Antonov, J. A. Caballero, M. B. Barbaro, and E. Moya de Guerra, *Phys. Lett. B* **711**, 178 (2012).
- [26] S. K. Singh, M. J. Vicente-Vacas, and E. Oset, *Phys. Lett. B* **416**, 23 (1998).
- [27] C. Praet, O. Lalakulich, N. Jachowicz, and J. Ryckebusch, *Phys. Rev. C* **79**, 044603 (2009).
- [28] M. B. Barbaro, A. De Pace, and L. Fiume, *Universe* **7**, 140 (2021).
- [29] M. V. Ivanov, G. D. Megias, R. González-Jiménez, O. Moreno, M. B. Barbaro, J. A. Caballero, and T. W. Donnelly, *J. Phys. G* **43**, 045101 (2016).
- [30] D. Rein and L. M. Sehgal, *Ann. Phys. (N.Y.)* **133**, 79 (1981).
- [31] G. Fogli and G. Nardulli, *Nucl. Phys.* **B160**, 116 (1979).
- [32] P. A. Schreiner and F. von Hippel, *Phys. Rev. Lett.* **30**, 339 (1973).
- [33] K. Matsui, T. Sato, and T. S. H. Lee, *Phys. Rev. C* **72**, 025204 (2005).
- [34] E. Hernández, J. Nieves, and M. J. Vicente Vacas, *Phys. Rev. D* **87**, 113009 (2013).
- [35] M. Martini and M. Ericson, *Phys. Rev. C* **90**, 025501 (2014).
- [36] M. Kabirnezhad, *Phys. Rev. D* **97**, 013002 (2018).
- [37] M. Kabirnezhad, *Phys. Rev. C* **107**, 025502 (2023).
- [38] S. Nakamura, H. Kamano, and T. Sato, *Phys. Rev. D* **92**, 074024 (2015).
- [39] S. X. Nakamura, H. Kamano, and T. Sato, *Phys. Rev. D* **99**, 031301 (2019).
- [40] Osaka University, Website of the ANL-Osaka DCC model, <https://www.rcnp.osaka-u.ac.jp/~anl-osk/> (2021), last accessed October 2023.
- [41] N. Rocco, S. X. Nakamura, T.-S. H. Lee, and A. Lovato, *Phys. Rev. C* **100**, 045503 (2019).
- [42] J. Gonzalez-Rosa, G. Megias, J. Caballero, and M. Barbaro, *Phys. Rev. D* **105**, 093009 (2022).
- [43] G. D. Megias, J. E. Amaro, M. B. Barbaro, J. A. Caballero, and T. W. Donnelly, *Phys. Rev. D* **94**, 013012 (2016).
- [44] R. D. Ball, V. Bertone, F. Cerutti, L. Del Debbio, S. Forte, A. Guffanti, J. I. Latorre, J. Rojo, and M. Ubiali (NNPDF Collaboration), *Nucl. Phys.* **B855**, 153 (2012).
- [45] J. D. Bjorken, *Phys. Rev.* **179**, 1547 (1969).
- [46] A. G. Tooran, A. Khorramian, and H. Abdolmaleki, *Phys. Rev. C* **99**, 035207 (2019).
- [47] A. Bodek, M. Breidenbach, D. L. Dubin, J. E. Elias, J. I. Friedman, H. W. Kendall, J. S. Poucher, E. M. Riordan, M. R. Sogard, D. H. Coward, and D. J. Sherden, *Phys. Rev. D* **20**, 1471 (1979).
- [48] A. Bodek and J. L. Ritchie, *Phys. Rev. D* **23**, 1070 (1981).
- [49] C. G. Callan and D. J. Gross, *Phys. Rev. Lett.* **22**, 156 (1969).
- [50] W. G. Seligman *et al.*, *Phys. Rev. Lett.* **79**, 1213 (1997).
- [51] J. H. Kim *et al.*, *Phys. Rev. Lett.* **81**, 3595 (1998).
- [52] T. Gehrmann, R. G. Roberts, and M. R. Whalley, *J. Phys. G* **25**, A1 (1999).
- [53] T. W. Donnelly and I. Sick, *Phys. Rev. Lett.* **82**, 3212 (1999).
- [54] J. E. Amaro, M. B. Barbaro, J. A. Caballero, R. González-Jiménez, G. D. Megias, and I. R. Simo, *J. Phys. G* **47**, 124001 (2020).
- [55] J. E. Amaro, M. B. Barbaro, J. A. Caballero, T. W. Donnelly, R. González-Jiménez, G. D. Megias, and I. Ruiz Simo, *Eur. Phys. J. Spec. Top.* **230**, 4321 (2021).
- [56] G. D. Megias, J. E. Amaro, M. B. Barbaro, J. A. Caballero, T. W. Donnelly, and I. R. Simo, *Phys. Rev. D* **94**, 093004 (2016).
- [57] G. D. Megias, M. B. Barbaro, J. A. Caballero, J. E. Amaro, T. W. Donnelly, I. R. Simo, and J. W. V. Orden, *J. Phys. G* **46**, 015104 (2018).
- [58] G. D. Megias, M. B. Barbaro, J. A. Caballero, and S. Dolan, *Phys. Rev. D* **99**, 113002 (2019).
- [59] G. D. Megias, T. W. Donnelly, O. Moreno, C. F. Williamson, J. A. Caballero, R. González-Jiménez, A. De Pace, M. B. Barbaro, W. M. Alberico, M. Nardi, and J. E. Amaro, *Phys. Rev. D* **91**, 073004 (2015).
- [60] I. R. Simo, J. E. Amaro, M. B. Barbaro, A. D. Pace, J. A. Caballero, and T. W. Donnelly, *J. Phys. G* **44**, 065105 (2017).

- [61] J. Amaro, M. Barbaro, J. Caballero, T. Donnelly, and C. Williamson, *Phys. Lett. B* **696**, 151 (2011).
- [62] G. D. Megias, Charged-current neutrino interactions with nucleons and nuclei at intermediate energies, Ph.D. thesis, University of Seville, 2017.
- [63] C. G. Callan and D. J. Gross, *Phys. Rev. Lett.* **22**, 156 (1969).
- [64] A. Bodek and U.-k. Yang, [arXiv:1011.6592](https://arxiv.org/abs/1011.6592).
- [65] A. G. Tooran, A. Khorramian, and H. Abdolmaleki, *Phys. Rev. C* **99**, 035207 (2019).
- [66] A. Bodek and J. L. Ritchie, *Phys. Rev. D* **24**, 1400 (1981).
- [67] S. Stein, W. B. Atwood, E. D. Bloom, R. L. A. Cottrell, H. DeStaebler, C. L. Jordan, H. G. Piel, C. Y. Prescott, R. Siemann, and R. E. Taylor, *Phys. Rev. D* **12**, 1884 (1975).
- [68] Y. Liang *et al.* (Jefferson Lab Hall C E94-110 Collaboration), *Phys. Rev. C* **105**, 065205 (2022).
- [69] M. Glück, E. Reya, and A. Vogt, *Eur. Phys. J. C* **5**, 461 (1998).
- [70] P. E. Bosted and M. E. Christy, *Phys. Rev. C* **77**, 065206 (2008).
- [71] S. P. Malace *et al.* (Jefferson Lab E00-115 Collaboration), *Phys. Rev. C* **80**, 035207 (2009).
- [72] G. D. Megias, J. E. Amaro, M. B. Barbaro, J. A. Caballero, and T. W. Donnelly, *Phys. Lett. B* **725**, 170 (2013).
- [73] E. L. Lomon, *Phys. Rev. C* **64**, 035204 (2001).
- [74] E. L. Lomon, *Phys. Rev. C* **66**, 045501 (2002).
- [75] C. Crawford *et al.*, *Phys. Rev. C* **82**, 045211 (2010).
- [76] O. Benhar, D. Day, and I. Sick, [arXiv:nucl-ex/0603032](https://arxiv.org/abs/nucl-ex/0603032).
- [77] L. Alvarez-Ruso *et al.* (GENIE Collaboration), *Eur. Phys. J. Spec. Top.* **230**, 4449 (2021).
- [78] Y. Hayato, *Acta Phys. Pol. B* **40**, 2477 (2009).
- [79] Y. Hayato and L. Pickering, *Eur. Phys. J. Spec. Top.* **230**, 4469 (2021).
- [80] R. González-Jiménez, M. B. Barbaro, J. A. Caballero, T. W. Donnelly, N. Jachowicz, G. D. Megias, K. Niewczas, A. Nikolakopoulos, and J. M. Udías, *Phys. Rev. C* **101**, 015503 (2020).
- [81] M. Martini, M. Ericson, and G. Chanfray, *Phys. Rev. C* **106**, 015503 (2022).